Printed in the Republic of Korea

ANALYTICAL SCIENCE & TECHNOLOGY

Vol. 39 No. 5, 290-304, 2026

https://doi.org/10.5806/AST.2026.39.5.290

Anomalous AC electrical transport and dielectric relaxation in vacuum-evaporated bi-oriented (301)/(322) Gd_2O_3Thin Films with Enhanced Surface Wettability

F. Trabelsi[1], I. H. Sharqi[1], and H. Dhaouadi[1,★], and Abdelwaheb Boukhachem[2]

[a]Laboratory of Soft Matter Physics and Fluid Physics (LP2MPF), Faculty of Sciences of Tunis, Université Tunis El-Manar, Campus UniversitaireFarhatHached, Tunis 2092, Tunisia

[b]Laboratoire Nanomateriaux et Systemes pour Les Energies Renouvelables (LANSER), Centre de Recherches et des Technologies de L'Energie Technopole BorjCedria, Bp 95, Hammam Lif 2050, Tunisia

(Received June 20, 2026; Revised September 7, 2026; Accepted October 12, 2026)

Abstract: Thin films of gadolinium oxide (Gd_2O_3, ~650 nm) were successfully deposited on glass substrates by vacuum thermal evaporation at a base pressure of 10^{-5} Torr.The structural study by X-ray diffraction (XRD) confirmed the presence of a single-phasecubic C-type rare-earth sesquioxide structureexhibiting two preferred orientations along the (301) and (322) planes, with an average crystallite size ranging from 100.31 to 145.35 nm. Field-emission scanning electron microscopy (FE-SEM) confirmed a dense, non-porous granular structure with a predominant grain size concentrated near 100 nm. Optical measurements revealed high transmittance (78–85 %) across the visible and near-infrared ranges, accompanied by a direct fundamental band gap of 4.05 eV and an Urbach energy of 0.31 eV, reflecting high structural order within the crystalline domains.The refractive index dispersion ($n \approx 2.08$–2.13) was accurately determined using Cauchy and Wemple–DiDomenicomodels, yielding a dispersion energy (E_d) of 22.99 eV. Temperature-dependent dielectric analysis revealed a prominent space charge polarization at low frequencies, obeying the Maxwell–Wagner–Sillars (MWS) polarizationlaw. The AC conductivity spectra followed Jonscher's power law, with an anomalous frequency exponent exceeding unity ($1.91 \leq s \leq 2.20$) increasing with temperature, indicating that cooperative hopping and mixed conduction of ions and electrons, mediated by doubly ionized oxygen vacancies (Vö), dominate the AC electrical transport. Furthermore, static contact angle measurements yielded a value of $\theta = 62°$, indicating moderate hydrophilicity and high surface free energy. These interrelated optical, insulating and conductive properties confirm the suitability of vacuum-evaporated Gd_2O_3 films for high-k dielectric applications, photovoltaic coatings, and surface-active sensors.

Keywords: Gd_2O_3 thin films, X-ray diffraction, dielectric spectroscopy, optical properties, electrical conductivity, wettability.

★ Corresponding author
Phone : +216-21-346-812
E-mail : hassen.dhaouadi@ipeit.rnu.tn

This is an open access article distributed under the terms of the Creative Commons Attribution Non-Commercial License (http://creativecommons.org/licenses/by-nc/3.0) which permits unrestricted non-commercial use, distribution, and reproduction in any medium, provided the original work is properly cited.

1. Introduction

Rare-earth oxides (REOs) have emerged as pivotal functional materials for next-generation microelectronics, optoelectronic devices, and protective optical coatings owing to their outstanding thermodynamic stability, high dielectric constants (k), and wide band gaps.[1,2] Among them, gadolinium oxide (Gd_2O_3) stands out as a promising candidate to as an alternative to conventional SiO_2 in high-k gate dielectric stacks, optical filters, and luminescent/magnetic dual-mode biomedical probes.[3-7] Bulk Gd_2O_3 typically exhibits three major polymorphs: cubic (bixbyite-type, space group Ia-3), monoclinic (C^2/m), and hexagonal (P6_3/mmc), with phase transitions occurring above 1473 K and 2443 K, respectively.[3,4] While bulk cubic Gd_2O_3 possesses a wide direct band gap of ~5.2 eV[8] and a high relative permittivity ($\varepsilon r \sim 16$), the physical properties of nanostructured Gd_2O_3 thin films are highly sensitive to deposition parameters, stoichiometric defects, crystallite orientation, and grain boundary structures.[9-12]

Thin films of Gd_2O_3 have been synthesized using various deposition techniques, including sol-gel processing,[17-21] electron-beam evaporation,[22-24] and thermal evaporation,[25] pulsed laser deposition (PLD),[26-29] atomic layer deposition (ALD).[30,31] Vacuum thermal evaporation offers distinct advantages, including high purity, simplicity, good control over stoichiometry, and excellent film uniformity. Despite extensive research on single-crystal and randomly oriented polycrystalline Gd_2O_3 films, the relationships among dual preferred crystallographic orientations (texture), point defects such as oxygen vacancies, and the resulting optical, dielectric, and surface-energy properties remains insufficiently explored. Of particular interest is the anomalous AC electrical transport mechanisms with a Jonscher's power- law exponent exceeds unity ($1.91 \leq s \leq 2.20$), which remains insufficiently understood and requires further investigation to elucidate its underlying physical behavior. In this study, we report a comprehensive investigation of bi-oriented (301) and (322) Gd_2O_3 thin films prepared by high-vacuum thermal evaporation. The crystallographic texture, surface morphology, defect-associated optical band gap narrowing (4.05 eV), Maxwell-Wagner-Sillars dielectric polarization, cooperative ion-hopping dynamics, and surface wettability were systematically investigated to establish a coherent structure-property relationship for device integration.

2. Experimental Details

2.1. Synthesis of Gd_2O_3 powder

Stoichiometric amounts of Gadolinium(III) chloride hexahydrate ($GdCl_3 \cdot 6H_2O$) and aqueous ammonia (NH_4OH, 99 % purity) were reacted in an aqueous solution to synthesize gadolinium hydroxide [$Gd(OH)_3$] precipitates according to the following chemical reaction.

$$GdCl_3 \cdot 6H_2O + 3NH_4OH \rightarrow Gd(OH)_3 \downarrow + 3NH_4Cl + 6H_2O$$

The resulting precipitate was collected by centrifugation, thoroughly washed with deionized water and ethanol to remove residual chloride ions, and dried at 100 °C. Thermal annealing was then performed to promote complete dehydration and phase transformation to Gd_2O_3.

$$2Gd(OH)_3 \xrightarrow{\Delta} Gd_2O_3 + 3H_2O \uparrow$$

Finally, the synthesized Gd_2O_3 powder was placed in a vacuum-sealed quartz tube and calcined at 600 °C

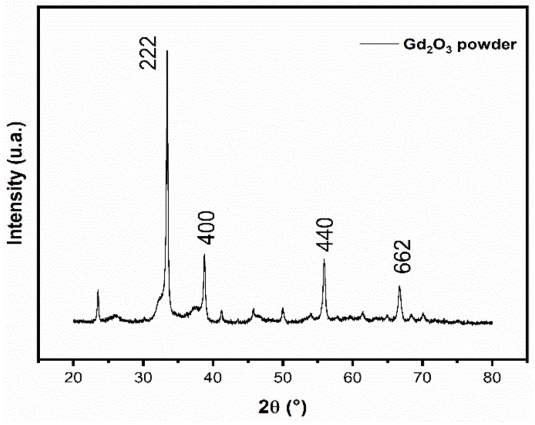


Fig. 1. XRD pattern of Gd_2O_3 powder prepared by chemical coprecipitation and calcined at 600 °C for 48 h.

for 48 h to obtain a well-crystallized cubic phase.

Fig. 1 shows theX-ray diffraction pattern ofthe Gd_2O_3 powder usedin this study. X'Pert High Score software analysis of the XRD patterns confirmes a single-phase cubic Gd_2O_3 structure belonging to the Ia-3 space group, consistent with JCPDS card No. 00-012-0797.

2.2. Preparation of Gd_2O_3 thin films

Thin films of gadolinium oxide (Gd_2O_3) were deposited onto pre-cleaned glass substrates using a vacuum thermal evaporation system equipped with a resistively heated molybdenum boat. Prior to deposition, the glass substrates were sequentially ultrasonically cleaned in acetone, then absolute ethanol, and finally deionized water for 15 min each, followed by drying with dry N_2 flow. The synthesized Gd_2O_3 powder was placed in the boat, and the chamber was evacuated to a basepressure of approximately 10^{-5} Torr. Deposition was carried out on fixed substrates at an elevated temperature of 500 °C at an average deposition rate of approximately 0.2 nm/s and was monitored in situ using a quartz crystal microbalance (QCM). After deposition, the samples were allowed to cool naturally to room temperature inside a vacuum chamber for 12 h to relieve thermal and residual stresses. The final film thickness was measured using a stylus surface profilometer (and cross-verified via optical reflectivity and spectroscopic ellipsometry) and determined to be approximately 650 nm.

2.3. Characterization techniques

Several investigation methods were used to study these samples. The crystal structure of every thin film produced was analyzed using a Philips PW 1729 Table-top X-ray Generator,with monochromatic radiation (Cu-Kα radiation, λ = 1.54059 Å), tests were carried out at room temperature. AJEOL-JSM 5400 SEM was used to determine grain size and surface morphology and microstructure.A spectrophotometer (Perkin-Elmer Lambda 950)with spectral domain 250–2500 nm was used to determine both optical reflectance (*R*) and transmittance (T) of the films,as functions of wavelength. AHewlett–Packard HP 4192 impedance

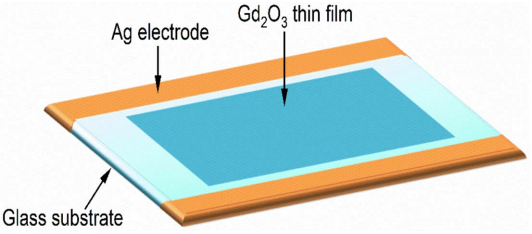


Fig. 2. Schematic illustration of the planarstructure of Ag/Gd_2O_3/Ag samples for the electrical and dielectric characterizations.

analyzer measuredthe dielectric and theelectrical properties of the films over a range of temperatures from 290–373 K and a frequency range of 1 Hz–1 MHz. As reported by Larbi *et al.*[35] the test configuration for the electrical measurements was two-electrodes attached to the two ends of the sample using conductive silver paste (*Fig.* 2).

Finally, the surface freeenergy of thin films at room temperature was deduced from the sessile drop method by studying the contact angle of water.The symmetrical droplet profiles on the horizontal film surface were analyzed using the DSA100 drop shape analyzer (Krüss GmbH, Hamburg).[36] Static contact angle measurements were performed using highly purified deionized water (γL = 72.8 mN/m), via the sessile drop method under ambient conditions (20 ± 1 °C), relative humidity ~ 45 % with a calibrated droplet volume of 3 μL.

3. Results and Discussion

3.1. XRD Investigation

Fig. 3 presents the XRD pattern of the Gd_2O_3 thin film recorded using a Philips PW 1729 tabletop X-ray generator (Cu-Kα radiation, λ = 1.5406 Å) with a 2θ scanning step of 0.02°. Two distinct diffraction peaks were observed at 2θ = 26.12° and 39.54°, which were indexed to the (301) and (322) crystallographic planes, respectively. The observed diffraction peaks are consistent with the cubic phase of Gd_2O_3 (space group $Ia\bar{3}$), in agreement with the standard JCPDS card No. 00-012-0797 and previously reported studies.[37-40] The interplanar spacing d_{hkl} was calculated

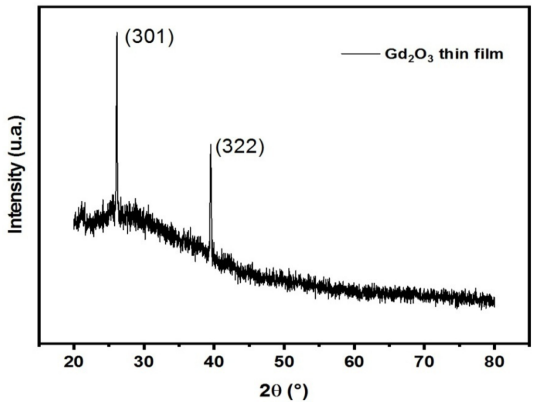


Fig. 3. X-ray diffractionpattern of Gd_2O_3 thin film.

using Bragg's law.

$$2d_{hkl}\sin\theta = n\lambda \quad (1)$$

where n is the order of the diffraction (usually = 1) and λ is the X-ray wavelength.

The lattice parameter (a) for the cubic structure was determined using the relation.[41]

$$d_{hkl} = \frac{a}{\sqrt{h^2+k^2+l^2}} \quad (2)$$

Values of the lattice parameters asdeduced from the two obtained diffraction peaks are given in *Table* 1. These values agreewellwith those given by the International Centre for Diffraction Data (JCPDS 00-012-0797 card) and previous results obtained by Artini *et al.*[42] and Delacotte *et al.*[43] In addition, the crystallite size (D), microstrain (ε), and dislocation density (δ) were calculated according to Eqs. (3)–(5).[44,45]

$$D = \frac{k\lambda}{\beta_{\frac{1}{2}}\cos\theta} \quad (3)$$

$$\varepsilon = \frac{\beta_{\frac{1}{2}}}{4\tan\theta} \quad (4)$$

$$\delta = \frac{1}{D^2} \quad (5)$$

Their values are summarized in *Table* 2.

In comparison with gadolinium and oxygen atomic radii, it is found that the lattice parameter (a) is relatively large due to the high number of Gd_2O_3 formula units per unit cell. *Fig.* 4(a) shows the Gd_2O_3 lattice in the cubic structure. In this structure, Gd^{3+}

Table 1. Lattice parameter of Gd_2O_3 thin film for (301) and (322) planes.

	(301)	(322)	00-012-0797JCPDS card	Shugurov *et al.*, 2025	Larbi *et al.*, 2014
a(Å)	10.7761	10.6853	10.8130	10.8175	10.8113

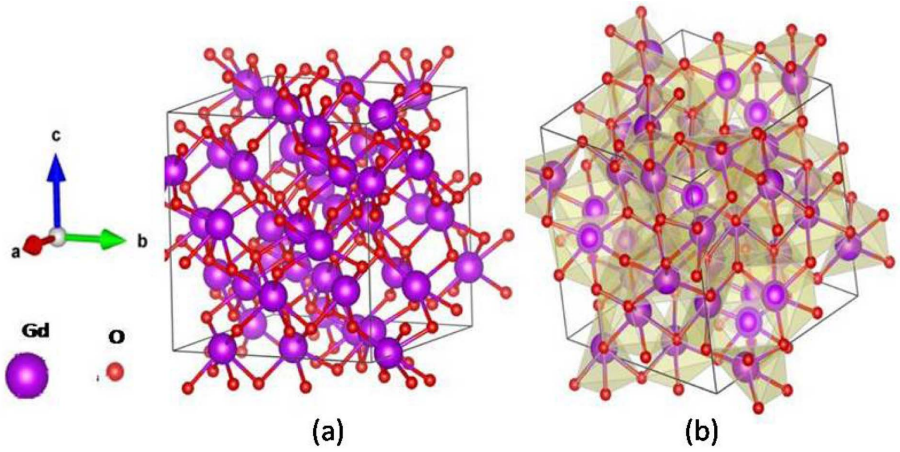


Fig. 4. (a) Unit cell representation of the Gd_2O_3 cubic crystal structure. (b) Coordination polyhedra of Gd.

Table 2. Structural parameters of Gd_2O_3 thin film for (301) and (322) planes.

Plane (hkl)	D (nm)	$(10^{-4})\varepsilon$	δ (10^{13} lines/m^2)
(301)	145.35	10.55	4.73
(322)	100.31	10.22	9.94

ions occupy the centers of octahedra cavities, while O^{2-} ions occupy the vertices of these octahedral *Fig.* 4(b).

3.2. Surface morphology of thin film

Fig. 5 illustrates the FESEM micrographs of the deposited Gd_2O_3 thin film recorded at different magnifications. Low-magnification micrographs (*Figs.* 5(a) and 5(b)) reveal a compact, crack-free, and homogeneous surface coverage across the substrate. At higher magnifications (*Figs.* 5(c) and 5(d)), well-defined polygonal grains and localized aggregates are clearly visible. The observed granular morphology is consistent with the typical nanocrystalline nature of Gd_2O_3 thin films, where the resulting microstructure is governed by deposition and heat treatment conditions.[44] Furthermore, the distinct, faceted grain boundaries support a polycrystalline structure and a preferred crystallographic orientation, indicated by the sharp (301) and (322) diffraction peaks. To gain a quantitative understanding of grain dimensions, the grain size distribution extracted from the surface topography is shown in *Fig.* 6. The distribution is relatively broad, ranging from several tens of nanometers to ~ 250 nm, with a prominent peak centered at around 100 nm. This confirms that the thin film is composed primarily of nanograins along with a small proportion of larger aggregates. The predominant grain size (~ 100 nm) obtained from field-emission scanning electron microscopy (FESEM) analysis closely matches the crystallite sizes ($D \approx$ 100.31–145.35 nm) determined from XRD data using the Scherrer equation. The presence of grains exceeding the crystallite size determined from the XRD data is expected, as individual grains often consist of multiple coherently

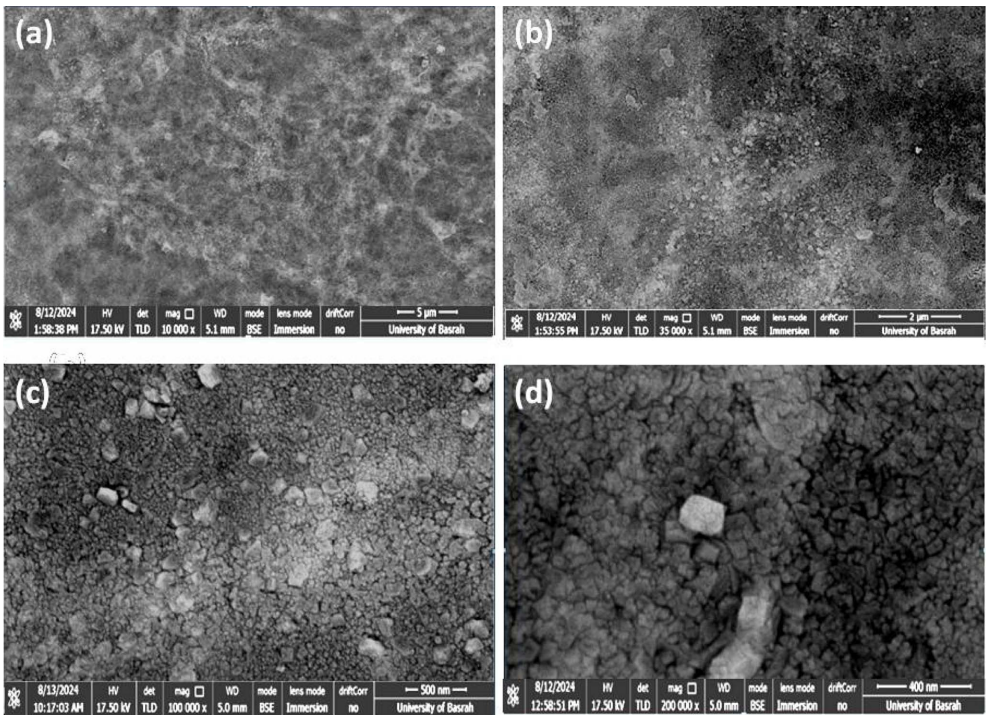


Fig. 5. FE-SEM images of Gd_2O_3 thin film surfaceat different magnifications.

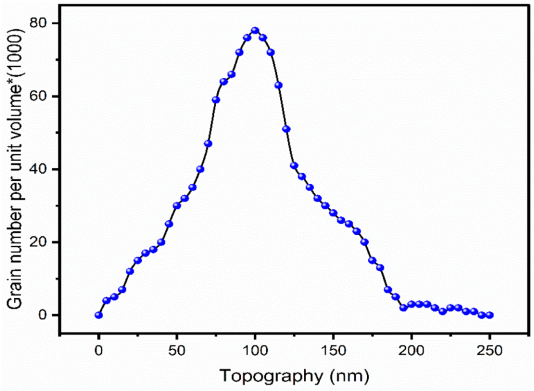


Fig. 6. Grain size distribution of the synthesized Gd_2O_3 thin film.

diffracting domains. Overall, the dense grain coverage in *Fig*. 6, along with the peak size distribution around 100 nm, confirms the successful growth of a coherent Gd_2O_3 thin film.

3.3. Optical properties

3.3.1. Absorption, transmission, and reflection spectra

The optical properties of the thin film fabricated from gadolinium oxide (Gd_2O_3) were evaluated using UV–Vis–NIR spectroscopy.As illustrated in *Fig*. 7(a), strong optical absorption is observed in the short-wavelength spectral region ($\lambda < 500$ nm), reaching a maximum near the fundamental absorption edge (400–450 nm). This strong absorption is primarily attributed to electronic transitions between energy bands, from the occupied O *2p* valence band to the unoccupied Gd*5d/4f* conduction band. As the wavelength extends into the visible region (500–750 nm), the absorption drops sharply to near-zero values, indicating minimal absorption of photons below the band gap and high optical transparency. The slight localized absorption observed around 800 nm can be attributed to instrumental effects or to localized states below the band gap resulting from oxygen vacancies. The transmittance (T%) and reflectance (R%) spectra (*Fig*. 7(b)) cover a wide range of wavelengths (200–2000 nm). In the ultraviolet region ($\lambda < 300$ nm), the transmittance approaches zero, consistent with strong band-gap-related absorption. A sharp transition begins between 350 and 600 nm, after which the film exhibits high optical transparency with an average transmittance of 78 %–85 % in the visible and near-infrared ranges.[45] Simultaneously, the reflectance (*R*%) remains consistently low (around 10–15 %) across the entire spectral window, with a characteristic detector-switching artifact near 860 nm. The combination of a sharp absorption edge, high visible transparency (> 80 %), and low reflectance confirms that the deposited Gd_2O_3 thin film possesses high crystalline quality with low scattering losses and minimal absorption due to defects. These optical

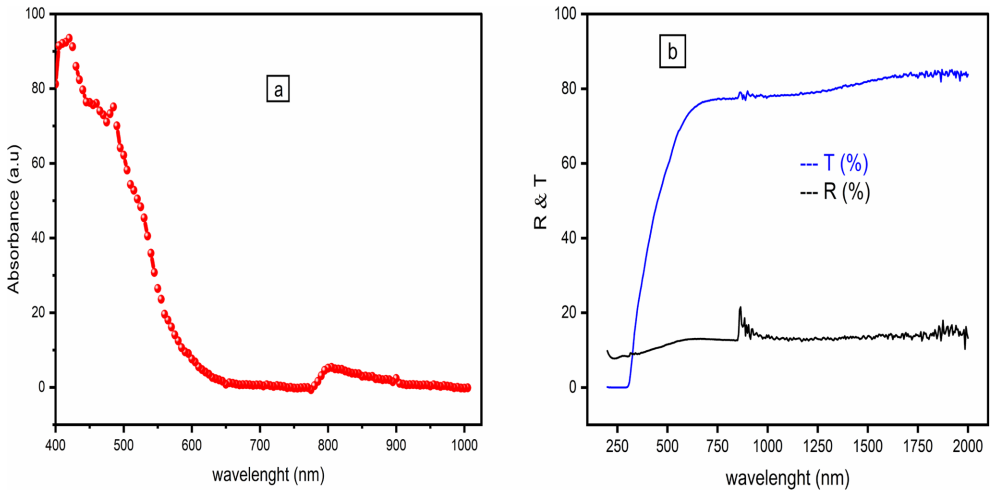


Fig. 7. Optical spectra of the Gd_2O_3 thin film: (a) absorbance spectrum, and (b) transmittance (*T*%) and reflectance (*R*%) spectra.

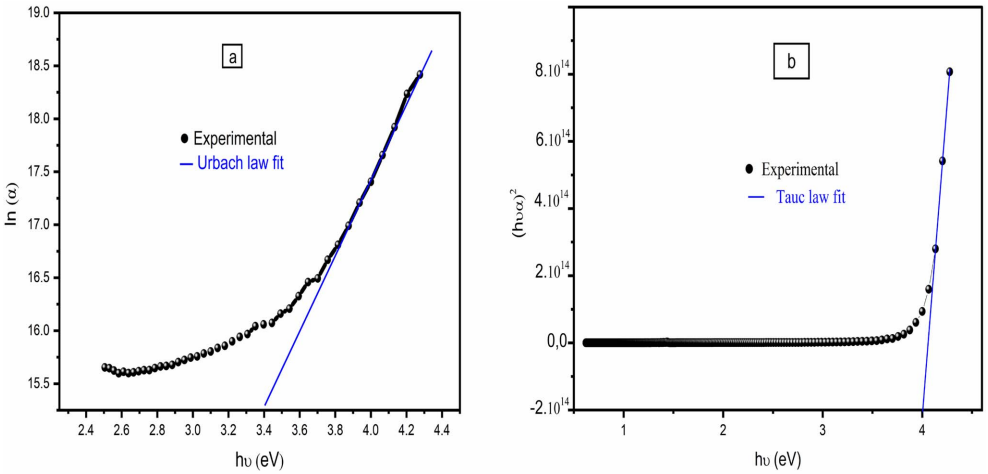


Fig. 8. Urbach and Tauc analyses of the Gd_2O_3 thin film: (a) Urbach plot and (b) direct optical band-gap determination.

properties make Gd_2O_3 thin films highly suitable as transparent dielectric thin films, UV photodetectors, and anti-reflective coatings in photovoltaic and photonic assemblies.

3.3.2. Energy band gap and urbach energy (E_U) calculations

To explore the mechanism of electronic transition and structural disorder near the edge of the optical band, the absorption coefficient (α) was determined using the relation α = 2.303A/t, where A is the absorbance and t is the film thickness. The incident photon energy (hv) was obtained from the fundamental relation hv = hc/λ. These parameters facilitate the evaluation of the band tail effect and the fundamental optical transition threshold in the fabricated thin films. The Urbach energy (E_U) of the low-energy exponential absorption tail was evaluated using the empirical relationship.[48]

$$\alpha = \alpha_o \exp\left(\frac{hv}{E_U}\right) \tag{6}$$

Taking the natural logarithm of both sides yields.

$$\ln(\alpha) = \ln(\alpha_o) + \frac{hv}{E_U} \tag{7}$$

where α_o is a constant, and E_U represents the width of the exponential absorption tail. Thus, E_U is obtained from the inverse slope of the linear segment of the graph ln(α) versus hv shown in *Fig.* 8(a).

$$E_U = \left(\frac{d\ln(\alpha)}{d(hv)}\right)^{-1} \tag{8}$$

Linear fitting in *Fig.* 8(a) gives an Urbach energy of ≈ 0.31 eV. This narrow exponential band tail reflects a low density of localized defect states and minimal structural disorder near the band edges.[48,50] Subsequently, the optical band gap was estimated using Tauc relation.

$$(\alpha hv)^n = B(hv - E_g) \tag{9}$$

where B is a material-dependent constant, E_g is the optical band-gap energy, and n depends on the nature of the electronic transition. For a direct allowed transition, n = 2, giving

$$(\alpha hv)^2 = B(hv - E_g) \tag{10}$$

Extrapolating the linear portion of the $(\alpha hv)^2$ curve versus hv to $(\alpha hv)^2 = 0$ (*Fig.* 8) establishes a direct optical band gap of $E_g \approx 4.05$ eV. This optical limit directly corresponds to the electronic interband transitions from the filled O *2p* valence band to the empty Gd 5d/4f conduction band.[50] The large defined band gap (4.05 eV) and the limited Urbach tail (0.31 eV) closely confirm the high crystal quality and predominant crystal size (100.31–145.35 nm)

calculated from X-ray diffraction data, as well as the dense and compact grain arrangement observed in the FESEM (*Figs.* 5 and 6). The well-defined crystalline domains suppress the scattering of grain boundary defects and bandgap-free transitions, confirming the successful formation of a highly coherent and transparent Gd_2O_3 insulating layer suitable for deep UV photovoltaic integration.[48-51] The measured optical band gap of the deposited thin films (E_g = 4.05 eV) is noticeably narrower than the value typically reported for bulk single-crystal Gd_2O_3) ~5.2 eV).[8] This band gap reduction can be attributed tothree interrelated physical mechanisms:

• **Oxygen Vacancy Sub-Bands:** Vacuum thermal evaporation under a base pressure of 10^{-5} Torr naturally leads to the emergence of sub-stoichiometric oxygen vacancies (Vö). These vacancy defects generate localized donor levels below the conduction band minimum (Gd 5d/4f), effectively inducing band-tailingand narrowing the optical transition threshold.

• **Urbach Band-Tail States:** The presence of structural disorder and localized states near the band edges is quantitatively supported by the extracted Urbach energy (E_U = 0.31eV).

• **Nanocrystalline Grain Boundary Effects:**The high density of grain boundaries within the nano-granular matrix (~100 nm) leads to internal microstrain (≈ 10.22 * 10^{-4}), this leads to possible local fluctuations that increase the shift of the optical absorption edge towards lower energies.

3.3.3. Optical constants and dispersion analysis

The complex refractive index ($n' = n + ik$) determines the optical response and wave propagation withinthe Gd_2O_3 thin film. The extinction coefficient (k), which describes the optical attenuation per unit distance, was calculated using the relationship.[52]

$$k = \frac{\alpha\lambda}{4\pi} \tag{11}$$

where α is the optical absorption coefficient and λ is the incident wavelength. Using the experimental reflectance coefficient (R) and the extinction coefficient (k), the refractive index (n) was obtained from Fresnel's relation.[52]

$$R = \frac{(n-1)^2 + k^2}{(n+1)^2 + k^2} \tag{12}$$

Fig. 10(a) illustrates the spectral evolution of the refractive index (n) and extinction coefficient (k) from 250 to 2000 nm. In the high-energy UV region (λ < 350 nm), the extinction coefficient (k) reaches a maximum value of approximately 0.40, indicating strong absorption between the fundamental energy bands across the optical band gap ($E_g \approx$ 4.05 eV). Beyond the fundamental absorption edge (λ > 550 nm), the extinction coefficient (k) drops sharply to negligible values (k < 0.05), confirming the high optical transparency (>80%) and minimal dispersion loss of the film. Simultaneously, the refractive index exhibits anomalous dispersion near the absorption edge, reaching a maximum value of approximately 2.13 at 650 nm, before stabilizing at normal dispersion across the near-infrared (NIR) region at a value of approximately 2.08. To quantitatively describe the dispersionbehavior in the transparent region (λ > 600 nm), the experimental refractive index was modeled using Cauchy's empirical dispersion relation.[53]

$$n(\lambda) = A + \frac{B}{\lambda^2} + \frac{C}{\lambda^4} \tag{13}$$

Furthermore, the refractive index (n) can be interpreted in terms of optical transitions using the single oscillator model of Wemple and Di-Domenico.[54]

$$n^2 - 1 = \frac{E_0 E_d}{E_0^2 - (h\nu)^2} \tag{14}$$

Where $h\nu$ is the incident photon energy, E_0 is the single-oscillator energy (representing the average

Table 3. Values of Cauchy parameters (A, B and C) and dispersion parameters E_0 and E_d for the Gd_2O_3 thin film.

	A	B (μm^2)	C (μm^4)	E_0 (eV)	E_d (eV)
Gd_2O_3 thin film	2.0755	0.0114	0.0661	7.0204	22.9961

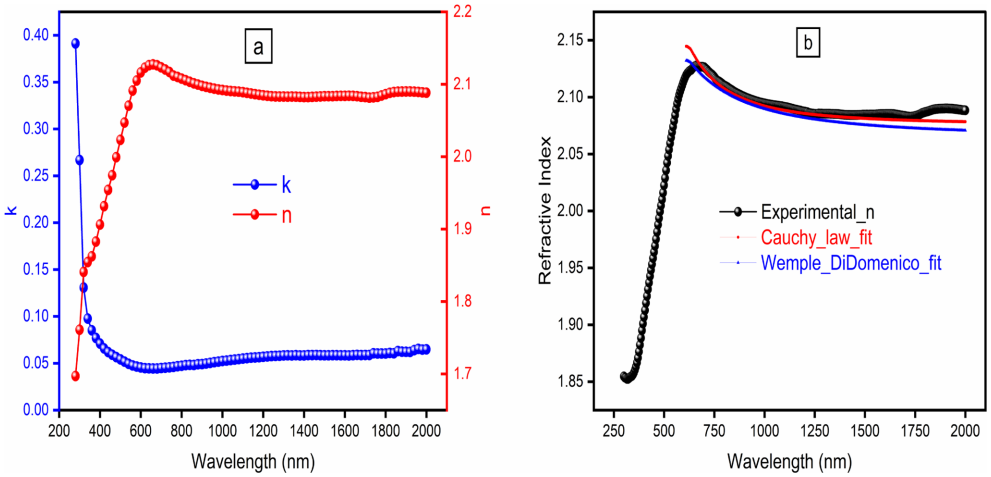


Fig. 9. Optical constants and dispersion analysis of the studied thin films: (a) extinction coefficient (k) and refractive index (n), and (b) refractive index fitting using the Cauchy and Wemple-DiDomenico models.

interband excitation energy), and E_d is the dispersion energy, which determines the average strength of the interband photon transitions. The coefficients extracted from the Cauchy relation and the Wemple-Di Domenico model are listed in *Table* 3.

As shown in *Fig.* 9(b), both the Cauchy and Wemple-Di Domenico models exhibit excellent agreement with experimental data in the normal dispersion regime. The high refractive index ($n \approx$ 2.08–2.13) directly reflects the high optical packing density and film cohesion. This is consistent with the morphology of dense, hole-free grains, confirmed by field-emission scanning electron microscopy (FESEM) (*Fig.* 5), and with the large crystallite dimensions verified by X-ray diffraction (*Fig.* 3), (100.31–145.35 nm). This high micropacking density leads to increased atomic polarization and a reduced internal void ratio, confirming the suitability of the prepared Gd_2O_3thin film as high-k dielectric layers and antireflective optical coatings.[52-54]

3.4. Electrical study

3.4.1. Dielectric study investigation

Figs. 10(a) and 10(b) illustrate the dependence of both the real part (ε') and the imaginary part (ε'') of the electrical permittivity of the Gd_2O_3 thin film on frequency and temperature, respectively. Both ε' and ε" were calculated using the following relationships.[55]

$$\varepsilon' = \frac{C.d}{\varepsilon_0 A} \tag{15}$$

$$\varepsilon'' = \varepsilon' \tan \delta \tag{16}$$

Where C is the capacitance, d is the film thickness, A is the electrode contact area, ε_0 is the permittivity of free space, and tan δ is the tangent of the dielectric loss angle.

At low frequencies (ln(f) < 8), both parameters exhibit high values that steadily decrease with increasing frequency until they reach a stable level. This behavior is consistent with the Maxwell-Wagner model of interfacial polarization and the Koops phenomenological theory.[55] Under the influence of an alternating field, thermally generated oxygen vacancies migrate through the conductive grains and accumulate at the resistive grain boundaries, generating a large space-charge polarization. At high frequencies, these dipoles are unable to keep pace with the rapid field oscillations, thus inhibiting the polarization response. The thermally assisted hoppingexplains the regular increase in permittivity with increasing temperature. These dielectric results are directly consistent with the dense, pinhole-free grain structure observed by field-emission scanning electron microscopy (*Fig.* 5) and with the pronounced diffraction peaks identified by

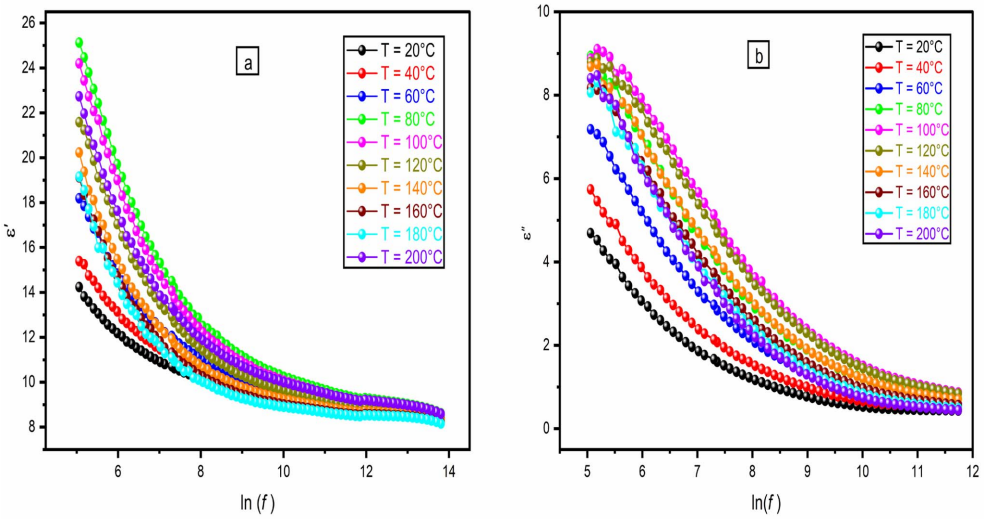


Fig. 10. Frequency and temperature dependence of the dielectric constant: (a) the real part (ε'), and (b) the imaginarypart (ε'') of the Gd_2O_3thin film.

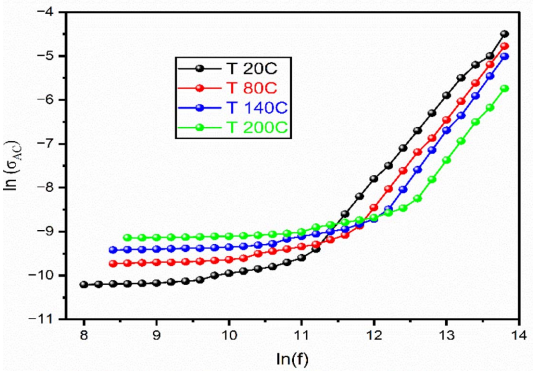


Fig. 11. AC conductivity as a function ofln(f) at different temperatures.

X-ray diffraction (*Fig.* 3), confirming the low leakage due to defects and reinforcing the high-*k* dielectric performance demonstrated by optical analysis.[55]

3.4.2. Electrical conductivity

The frequency dependence of total conductivity σ_{tot} for the Gd_2O_3 thin film at different temperatures (20 – 200 C) is shown in *Fig.* 11. The curves exhibit a frequency-independent DC plateau (σ_{dc}) at low frequencies (ln(f) < 11), followed by significant dispersion at higher frequencies where conductivity rises sharply.The experimental spectra were fitted using Jonscher's universal power law.[56]

$$\sigma_{tot}(\omega) = \sigma_{dc} + A\omega^{s} \quad (17)$$

where $\omega = 2\pi$ fis the angular frequency, A is a temperature-dependent pre-factor, and s is the frequency exponent. As illustrated in *Fig.* 12, the Jonscher model demonstrates an excellent fit with the experimental data. Charge transport is governed by thermally generated mobile oxygen vacancies (Vö). At low frequencies, these carriers hop over long distances across grain boundaries, establishing σdc .At higher frequencies, conduction shifts to short-range localized hopping between defect states, yielding AC dispersion.[56,57] The frequency exponent (s) exceeds unity and increases with temperature, confirming that cooperative hopping and ionic conduction dominate the transport mechanism.[57] These electrical characteristics correlate directly with the preceding structural, optical, and dielectric findings. The dense, pinhole-free morphology observed via FESEM (*Fig.* 5) along with the well-defined crystalline domains verified by XRD (*Fig.* 3) effectively suppress grain boundary scattering and defect-mediated leakage currents. Furthermore, the localized hopping centers correspond to the sub-band gap defect states quantified by E_U, where the high

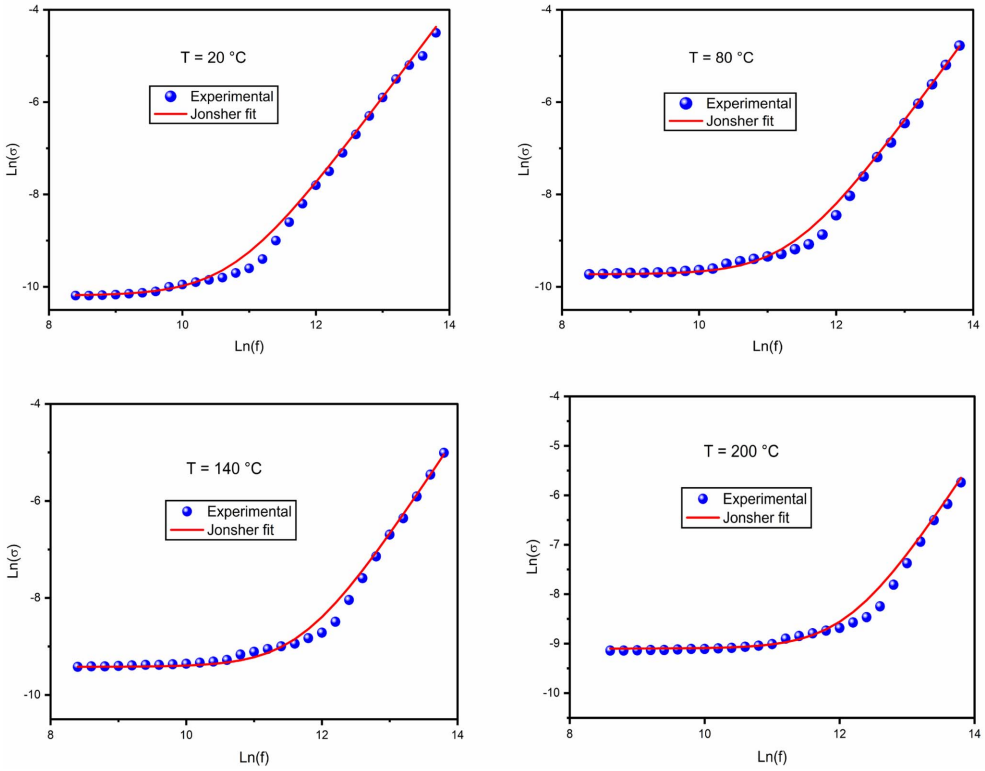


Fig. 12. Experimental AC conductivity spectra fitted with Jonscher's universal power law for the Gd_2O_3 thin film at (a) 20 C, (b) 80 C, (c) 140C, and (d) 200C.

electronic polarizability evidenced by the refractive index ($n \approx 2.08–2.13$) and oscillator strength (E_d) facilitates carrier hopping.[56,57] This transport behavior is fully consistent with the dielectric response, as the onset of conductivity dispersion coincides with the relaxation threshold of both ε' and ε'' *Fig.* 10, confirming that both conduction and interfacial polarization are mediated by the same mobile oxygen vacancy dynamics.

As can be seen from the fitting parameters in *Fig.* 12, the DC plateau extends and shifts toward higher frequencies as the temperature increases. This behavior confirms the thermally activated hopping conduction, where high thermal energy enables charge carriers to overcome local potential barriers, thereby shifting the onset of AC dispersion toward higher frequencies.

Additionally, from this Jonscher fit, the frequency exponent exceeds unity ($1.91 \leq s \leq 2.20$) and increases with temperature (*Fig.* 13). This increase is attributed to

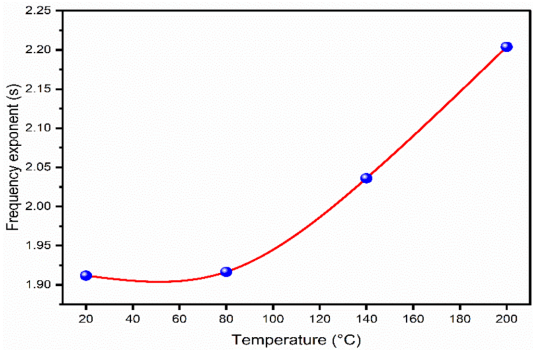


Fig. 13. Variation of the frequency exponent (s) with temperaturefor the Gd_2O_3 thin film.

mixed ionic and electronic conduction. The difference in electronegativity between gadolinium (1.2) and oxygen (3.44) is 2.24.Since this value is greater than 2, Gd_2O_3 has a predominantly ionic character, suggesting that ionic charge carriers contribute to electrical conduction.

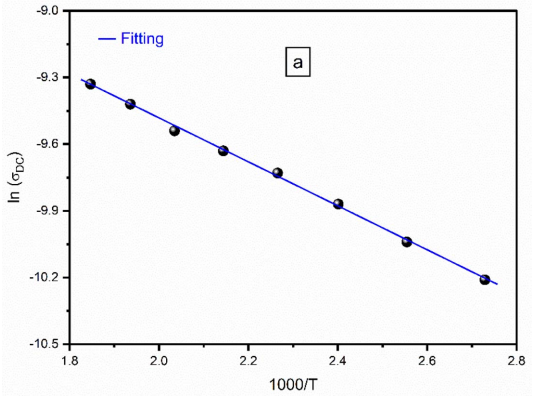


Fig. 14. Arrhenius plotof DC conductivity σ_{DC} versus 1000/T for the Gd_2O_3 thin film.

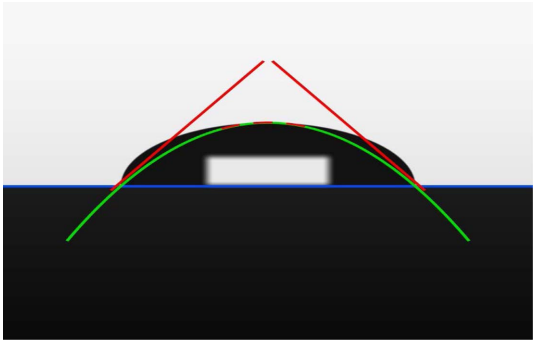


Fig. 15. Sessile drop profile and contact angle measurement on the surface of the Gd_2O_3thin film at room temperature) 20°C).

Fig. 14 presents the Arrhenius plot of $\ln(\sigma_{DC})$ versus 1000/T for thin films of Gd_2O_3. The DC conductivity increases monotonically with increasing temperature, demonstrating typical thermally activated semiconductor behavior according to the Arrhenius relation.

$$\sigma_{dc} = \sigma_0 \exp\left(-\frac{E_a}{k_B T}\right) \tag{18}$$

where σ_0 is the pre-exponential factor, E_a is the DC conduction activation energy, k_B is the Boltzmann constant, and T is the absolute temperature. The linear fit gives an activation energy of E_a = 0.53 ± 0.03 eV. This energy barrier corresponds to the enthalpy of ionized oxygen vacancy migration (Vö), confirming that thermally driven defect migration dominates DC electrical transport in the thin film.

3.5. Wettability properties

The wettability of the fabricated Gd_2O_3 thin film surface was assessed by measuring the static contact angle at an ambient temperature of 20 °C, as shown in *Fig.* 15. The geometrical profile fitting of the sessile water droplet resulted in a calculated contact angle (θ) of 62° over repeated measurements. Because the contact angle is lower than the hydrophobic threshold (θ < 90°), the Gd_2O_3 surface exhibits pronounced hydrophilic behavior, favoring effective liquid–solid interfacial interaction across the substrate surface. Thermodynamically, this low contact angle is associated with high surface free energy and strong interfacial adhesion forces between the solid and liquid.

This favorable wetting behavior indicates a high concentration of chemically active surface states, particularly oxygen vacancies (Vö) on the surface of Gd_2O_3. These defective sites facilitate photon absorption under UV illumination, promoting photochemical reactions and the subsequent generation of reactive oxygen species (ROS). Consequently, this enhanced surface interaction promotes efficient molecular adsorption, suggesting the potential of Gd_2O_3 thin films for heterogeneous photocatalysis, as well as high-performance chemical and biological sensors.[58] It should be noted that while a single polar liquid provides a qualitative assessment of surface wetting behavior, a comprehensive deconvolution into dispersive γ_s^d and polar γ_s^p components requires multi-liquid evaluations (e.g., Owens–Wendt approach), which remains a subject for future study.

4. Conclusions

Thin films of gadolinium oxide (Gd_2O_3) were successfully grown using vacuum thermal evaporation and comprehensively evaluated for their structural, optical, dielectric, electrical, and surface wetting properties. X-ray diffraction (XRD) and field emission scanning electron microscopy (FE-SEM) analysis

confirmedthe formation of a dense, well-crystallized cubic phase with two preferred crystallographic directions along (301) and (322) and a cohesive granular structure. Optically, the films exhibited high transparency in the visible light range (>80 %), a band gap of 4.05 eV, and a low Urbach energy (E_U = 0.31 eV), confirming minimallocalized band-tail states. The high refractive index dispersion and oscillator strength confirmed dense atomic packing. Dielectric spectroscopy revealed interfacial Maxwell–Wagner–Sillars (MWS) polarization resulting from charge carrier accumulation at the resistive grain boundaries. The conductivity spectra followed Jonscher's power law, with the frequency exponent s exceeding unity ($1.91 \leq s \leq 2.20$) and increasing with temperature.This anomalous transport behavior rules out simple single-polaron hopping models (such as CBH) and is attributed to cooperative ion-hopping dynamics facilitated by the strong ionic properties of Gd_2O_3 and mobile oxygen vacancies (Vö), as confirmed by the activation energy of 0.53 ± 0.03 eV. Finally, the moderate hydrophilicity ($\theta = 62°$) and good surface adhesion highlight the great potential of these bi-oriented Gd_2O_3 thin films for multifunctional integration in high-k gate dielectrics, UV-transparent optical coatings, and interfacial sensor platforms.

References

1. S. Murthy, P. Effiong, and C. Chin Fei, *Metal Oxide Powder Technologies*, **11**, 233-251 (2020). https://doi.org/10.1016/B978-0-12-817505-7.00011-7
2. R. Jbeli, A. Boukhachem, I. Ben Jemaa, N. Mahdhi, F. Saadallah, H. Elhouichet, S. Alleg, M. Amlouk, and H. Ezzaouïa, *SpectrochimicaActa Part A.*, **184**, 71-81 (2017) https://doi.org/10.1016/j.saa.2017.04.072
3. H. Jamnezhad and M. Jafari, *Journal of Magnetism and Magnetic Materials*, **408**, 164 (2016). https://doi.org/10.1016/j.jmmm.2016.02.041
4. F. X. Zhang, M. Lang, J. W. Wang, U. Becker, and R. C. Ewing, *Physical Review B*, **78**, 064114 (2008). https://doi.org/10.1103/PhysRevB.78.064114
5. M. Ahren, L. Selegard, F. Soderlind, M. Linares, J. Kauczor, P. Norman, P.O. Kall, and K. Uvdal, *Journal of Nanoparticle Research*, **14**, 1006 (2012). https://doi.org/10.1007/s11051-012-1006-2
6. T. Gayathri, N. M. Sundaram, and R. A. Kumar, *J. Bionanoscience*, **9**, 403-423 (2015). https://doi.org/10.1166/jbns.2015.1325
7. W. Yanli, X. Xianzhu, L. Qianlan, Y. Ruchun, D. Haixin, and X. Qiang, *Journal of Rare Earths*, **33**, 529 (2015). https://10.1016/S1002-0721(14)60452-X
8. M. Zinkevich, *Progress in Materials Science*, **52**, 597 (2007). https://doi.org/10.1016/j.pmatsci.2006.09.002
9. G. Bonnet, M. Lachkar, J. P. Larpin, and J. C. Colson, *Solid State Ionics*, **72**, 344 (1994). https://doi.org/10.1016/0167-2738(94)90171-6
10. N. K. Sahoo, S. Thakur, M. Senthilkumar, D. Bhattacharyya, and N. C. Das, *Thin Solid Films*, **440**, 155 (2003). https://doi.org/10.1016/S0040-6090(03)00678-3
11. M. Mishra, P. Kuppusami, S. Ramya, V. Ganesan, A. Singh, R. Thirumurugesan, and E. Mohandas. *Surface and Coatings Technology*, **262**, 56 (2015). https://doi.org/10.1016/j.surfcoat.2014.12.012
12. T. Echtermeyer, H. D. B. Gottlob, T. Wahlbrink, T. Mollenhauer, M. Schmidt, J. K. Efavi, M. C. Lemme, and H. Kurz, *Solid-State Electronics*, **51**, 617 (2007). https://doi.org/10.1016/j.sse.2007.02.016
13. T. M. Pan, C. Liao, H. Hsu, C. Chen, J. Lee, K. Wang, and J. Wang, *Applied Physics Letters*, **87**, 262908 (2005). https://doi.org/10.1063/1.2152150
14. Y. D. Zhen, A. I. Y. Tok, S. P. Jiang, and F. Y. C. Boey, *Journal of Power Sources*, **178**, 69 (2008). https://doi.org/10.1016/j.jpowsour.2007.11.113
15. S. K. Pandey, S. Singh, and S. K Mehta, *Journal of Colloid and Interface Science*, **529**, 496 (2018). https://doi.org/10.1016/j.jcis.2018.06.030
16. S. Roux, A. C. Faure, C. Mandon, S. Dufort, C. Riviere, J. L. Bridot, B. Mutelet, C. A. Marquette, V. Josserand, G. L. Duc, A. L. Pape, C. Billotey, M. Janier, J. L. Coll, P. Perriat, and O. Tillement, *Imaging in Medicine*, **2**, 211 (2010). https://doi.org/10.2217/iim.10.5
17. H. Guo, X. Yang, T. Xiao, W. Zhang, L. Lou, and J. Mugnier, *Applied Surface Science*, **230**, 215 (2004). https://doi.org/10.1016/j.apsusc.2004.02.032
18. M. C. Ferrara, D. Altamura, M. Schioppa, L. Tapfer, E. Nichelatti, L. Pilloni, and M. Montecchi, *Journal of Physics D: Applied Physics*, **41**, 225408 (2008). https://

doi.org/10.1088/0022-3727/41/22/225408
19. C. L. Luyer, A. García-Murillo, E. Bernstein, and J. Mugnier, *Journal of Raman Spectroscopy*, **34**, 234 (2003). https://doi.org/10.1002/jrs.980
20. Z. N. Kayani, Z. Bashir, M. Mohsin, S. Riaz, and S. Naseem, *Optik*, **243**, 167502 (2021). https://doi.org/10.1016/j.ijleo.2021.167502
21. R. Sivasamy, P. Venugopal, and E. Mosquera, *Vacuum*, **175**, 109255 (2020). https://doi.org/10.1016/j.vacuum.2020.109255
22. J. X. Wang, A. Laha, A. Fissel, D. Schwendt, R. Dargis, T. Watahiki, R. Shayduk, W. Braun, T. M. X. Liu, and H. J. Osten, *Semiconductor Science and Technology*, **24**, 045021 (2009). https://doi.org/10.1088/0268-1242/24/4/045021
23. S. Thakur, N. K. Sahoo, M. Senthilkumar, and R. B. Tokas, *Optical Materials*, **27**, 1402 (2005). https://doi.org/10.1016/j.optmat.2004.10.005
24. H. D. B. Gottlob, T. Echtermeyer, T. Mollenhauer, J. K. Efavi, M. Schmidt, T. Wahlbrink, M. C. Lemme, H. Kurz, M. Czernohorsky, E. Bugiel, H. J. Osten, and A. Fissel, *Solid State Electron*, **50**, 979 (2006). https://doi.org/10.1016/j.sse.2006.04.018
25. D. A. Grave, Z. R. Hughes, J. A. Robinso, T. P. Medill, M. J. Hollander, A. L. Stump, M. Labella, C. X. Weng, and D. E. Wolfe, *Surface and Coatings Technology*, **206,** 3094-3103 (2012). https://doi.org/10.1016/j.surfcoat.2011.12.016
26. K. S. Chang, L. Hsieh, S. Huang, C. Lee, and Y. Chiu, *Journal of Crystal Growth*, **310**, 1961 (2008). https://doi.org/10.1016/j.jcrysgro.2007.11.134
27. Y. Yulizar, A. Eprasatya, D. O. B Apriandanu, and R. T Yunarti, *Vacuum*, **183**, 109821 (2021). https://doi.org/10.1016/j.vacuum.2020.109821
28. R. K. Gupta, K. Ghosh, and P. K. Kahol, *Physica E*, 41, 1201 (2009). https://doi.org/10.1016/j.physe.2009.02.001
29. X. Cheng, D. Xu, Z. Song, D. He, Y. Yu, Q. Zhao, and D. Shen, *Applied Surface Science*, **256**, 921 (2009). https://doi.org/10.1016/j.apsusc.2009.08.086
30. A. Molle, S. Spiga, M.N.K. Bhuiyan, G. Tallarida, M. Perego, C. Wiemer, and M. Fanciulli, *Materials Science in Semiconductor Processing*, **11**, 236 (2008). https://doi.org/10.1016/j.mssp.2008.10.002
31. S. Duenas, H. Castan, H. Garcia, A. Gomez, L. Bailon, K. Kukli, T. Hatanpaa, J. Lu, M. Ritala, and M. Leskela, *Journal of The Electrochemical Society*, **154**, G207 (2007). https://doi.org/10.1149/1.2761845
32. J. McAlees, J. C. Plakatouras, and B. C. H. Steele, *Thin Solid Films*, **286**, 64 (1996). https://doi.org/10.1016/S0040-6090(96)08537-8
33. M. P. Singh and S. A. Shivashankar, *Journal of Crystal Growth*, **276**, 148 (2005). https://doi.org/10.1016/j.jcrysgro.2004.11.385
34. S. M. Shugurov, O. A. Zhinkina, E. A. Balabanova, D. A. Repin, and S. I. Lopatin, *Ceramics International*, **51**, 7202 (2025). https://doi.org/10.1016/j.ceramint.2024.12.154
35. T. Larbi, B. Ouni, A. Boukhachem, K. Boubaker, and M. Amlouk, *Materials Research Bulletin*, **60**, 457 (2014). https://doi.org/10.1016/j.materresbull.2014.08.020
36. J. Y. Heng, Y. A. Bismarck, and D. R. Williams, *AAPS Pharm. Sci. Tech.*, **7**, 84 (2006). https://doi.org/doi.org/10.1208/pt070484
37. F. Whba, F. Mohamed, N. R. Alia, M. Rosli, I. Abdul Rahman, and M. I. Idris, *Radiation Physics and Chemistry*, **179**, 109212 (2021). https://doi.org/10.1016/j.radphyschem.2020.109212
38. V. A. Pustovarov, R. E. Nikolaev, V. A. Trifonov, M. S. Tarasenko, S. J. Dhoble, D. A. Tavrunov, and N. G. Naumov, *Optical Materials*, **141**, 113966 (2023). https://doi.org/10.1016/j.optmat.2023.113966
39. B. D. Cullity and S. Rstock, "Elements of X-Ray Diffraction 3rd Ed.", Prentice Hall, New Jersey, (2001). ISBN-13: 978-0201610918
40. L.P. Peng, L. Fang, X. F. Yang, Y. J. Li, Q. L. Huang, F. Wu, and C.Y. Kong, *Journal of Alloys and Compounds*, **484**, 575 (2009). https://doi.org/10.1016/j.jallcom.2009.04.139
41. O. Lupan, T. Pauporté, L. Chow, B. Viana, F. Pellé, L. K. Ono, B. R. Cuenya, and H. Heinrich, *Applied Surface Science*, **256**, 1895 (2010). https://doi.org/10.1016/j.apsusc.2009.10.032
42. C. Artini, G. A Costa, M. Pani, A. Lausi, and J. Plaisier, *Journal of Solid State Chemistry*, **190**, 24 (2012). https://doi.org/10.1016/j.jssc.2012.02.002
43. C. Delacotte, T. A. Pomelova, T. Stephant, T. Guizouarn, S. Cordier, N. G. Naumov, and P. Lemoine, *Chemistry of Materials*, **34**, 1829 (2022). https://doi.org/10.1021/acs.chemmater.1c04105
44. M. C. Ferrara, D. Altamura, M. Schioppa, L. Tapfer, E.

Nichelatti, L. Pilloni, and M. Montecchi, *Journal of Physics D: Applied Physics*, **41**, 225408 (2008). https://doi.org/10.1088/0022-3727/41/22/225408.

45. A. Hafdallah, A. Azzedine, H. Belhani, M. Salah Aida, and N. Attaf, *American Journal of Nano Research and Applications*, **5**, 87 (2017). https://doi.org/10.11648/j.nano.20170506.12
46. M. M. F. de Azevedo, E. E. C. Costa, G. S. M. de Araújo, A. A. Hidalgo, and M. L. Vega, *Langmuir*, **42**, 11100-11112 (2026). https://doi.org/10.1021/acs.langmuir.5c06770.
47. R. Özmenteş and H. C. Vasconcelos, *Physica B: Condensed Matter*, **738**, 418761 (2026). https://doi.org/10.1016/j.physb.2026.418761
48. S. Bhakta, R. Panda, and P. K. Sahoo, *Scientific Reports*, **14**, 22767 (2024). https://doi.org/10.1038/s41598-024-69853-y.
49. A. S. Bhoir, S. D. Gunjal, A. S. Pathan, A. S. Landge, Y. V. Hase, B. M. Palve, D. L. Gapale, and S. A. Arote, *Next Materials*, **5**, 100272 (2024). https://doi.org/10.1016/j.nxmate.2024.100272.
50. M. M. El-Desoky, M. E. Abd-Elrazek, A. M. Elseman, and I. Morad, *AppliedPhysics A*, **131**, 402 (2025). https://doi.org/10.1007/s00339-025-08493-z.
51. Y. A. Kuznetsova, D. A. Zatsepin, A. F. Zatsepin, and N. V. Gavrilov, *Journal of Alloys and Compounds*, **904**, 163872 (2022). https://doi.org/10.1016/j.jallcom.2022.163872
52. M. Dongol, M. M. El-Nahass, H. S. Metwally, and A. A. Hassan, *Physica B: Condensed Matter*, **639**, 414008 (2022). https://doi.org/10.1016/j.physb.2022.414008
53. K. S. Urmila, T. A. Namitha, and R. Philip, *Optical Materials*, **131**, 112711 (2022). https://doi.org/10.1016/j.optmat.2022.112711
54. A. S. Al-Asadi, F. K. Yam, and K. P. Beh, *AppliedPhysics A*, **129**, 347 (2023). https://doi.org/10.1007/s00339-023-06634-1
55. S. Sen, R. Kumar, and A. Sharma, *Journal of Materials Science: Materials in Electronics*, **34**, 1045 (2023). https://doi.org/10.1007/s10854-023-10452-1
56. N. A. Okereke, C. M. Iroegbu, and E. O. Agbogu, *Journal of Alloys and Compounds*, **960**, 170685 (2023). https://doi.org/10.1016/j.jallcom.2023.170685
57. H. R. Fadhil, M. A. Kadhim, and S. B. Aziz, *Physica B: Condensed Matter*, **674**, 415582 (2024). https://doi.org/10.1016/j.physb.2023.415582
58. X. Wang, Y. Zhao, and T. Zhang, *ACS Applied Materials & Interfaces*, **13**, 16520-16531 (2021). https://doi.org/10.1021/acsami.1c03450